The eruption run-up at Mt. Etna volcano: constraining magma decompression rates and their relationships with the final eruptive energy

Francesco Zuccarello[1,2], Federica Schiavi[3], Marco Viccaro[1,2]

[1] Istituto Nazionale di Geofisica e Vulcanologia – Sezione di Catania, Osservatorio Etneo, Piazza Roma 2, I-95125, Catania, Italy

[2] Università degli Studi di Catania, Dipartimento di Scienze Biologiche Geologiche e Ambientali, Corso Italia 57, I-95129, Catania, Italy

[3] Université Clermont-Auvergne, CNRS, IRD, OPGC, Laboratoire Magmas et Volcans, F-63000, Clermont-Ferrand, France

Correspondence M. Viccaro, Università degli Studi di Catania, Dipartimento di Scienze Biologiche Geologiche e Ambientali, Corso Italia 57, I-95129, Catania, Italy. Email: m.viccaro@unict.it

Abstract

Although explosivity is linked with high decompression rates induced by magma ascent, the quantitative relationships between decompression rate and eruption energy have yet to be properly assessed, especially for open-conduit basaltic volcanoes, where ordinary weak activity can rapidly evolve into more intense eruptions. Here, we selected three eruptions of different explosivity from Mt. Etna's recent activity to study the relationships between the observed explosive intensities and decompression rates determined through diffusion chronometry, which is based on modeling volatile diffusion along olivine-hosted melt embayments. The approach used in this study has provided important indications on differences in the timescales of decompression-driven degassing for magmas emitted with markedly distinct eruptive dynamics, starting from similar physical and chemical conditions of the magmas involved in the three eruptions. The intense paroxysmal activity at Voragine Crater on December 3, 2015, was fostered by high decompression rate (~0.36-0.74 MPa/s), slightly higher than in the less energetic paroxysm that occurred on February 19, 2013, at New South-East Crater (NSEC) (~0.14-0.29 MPa/s). Decompression rates of magmas emitted during lava fountaining are one order of magnitude greater than values obtained for the mild flank eruption that occurred in December 2018 (~0.045-0.094 MPa/s). Our results indicate that degassing kinetics controlled the intensity of activity at Mt. Etna, thus suggesting that the explosivity does not depend exclusively on

the degree of overpressurization of the shallowest reservoir due to injection of gas from the deepest levels of the plumbing system.

Keywords: Mt. Etna; decompression rate; melt embayment; diffusion modeling; explosivity.

1. Introduction

The relatively low viscosity of magmas erupted at basaltic volcanoes generally promotes effusive or weak explosive activity (i.e., Hawaiian and Strombolian). However, basaltic volcanoes can also show more explosive behavior, occasionally Plinian/Subplinian style (Williams, 1983; Walker, 1984; Coltelli et al., 2000, Pérez et al., 2009; Lloyd et al., 2014). Highly explosive eruptions represent the major source of hazard at basaltic volcanoes, but the dynamics of magmatic processes and triggering mechanisms of these unusual eruptive phenomena are still poorly understood. Furthermore, the unexpected character of these events makes it difficult to correctly interpret precursory signals available from monitoring systems, especially at open-system volcanoes characterized by almost persistent activity, where the origin of such signals may be controversial.

Several studies attempted to decipher the processes and factors leading to increased energy during explosive basaltic eruptions (Houghton et al., 2004; Allard et al., 2005; Lloyd et al., 2014; Moretti et al., 2018; Arzilli et al., 2019; La Spina et al., 2021). These studies focused on the role of conduit processes, degassing dynamics, volatile flushing, groundmass crystallization and magma ascent rates. In particular, the decompression rate induced by syn-eruptive magma ascent is believed to be crucial in controlling the explosive intensity of an eruption with respect to other factors (e.g., melt viscosity, crystallinity, conduit geometry). Syn-eruptive ascent not only determines the exsolution of volatiles induced by pressure drop, resulting in increased magma buoyancy, but also controls the style of magma degassing (i.e. equilibrium vs. disequilibrium degassing) and the kinetics of bubble nucleation, growth and coalescence, in turn determining the volatile overpressure (Mangan and Cashman, 1996; Mourtada-Bonnefoi and Laporte, 2004; Gonnermann and Manga, 2007; Rutherford, 2008). Inertial fragmentation or fluid-dynamic breakup of low-viscosity melts are induced by rapid expansion of bubbles at high decompression rate (Mangan and Cashman, 1996; La Spina et al., 2021). Kinetics of syn-eruptive degassing also has a significant effect on the rheological properties of the magma, which depend mainly on crystallinity (which may increase due to ascent-driven crystallization of the groundmass), the presence of bubbles not escaping from the melt, temperature variations, and the increase in melt polymerization due to volatile exsolution. Such parameters strongly control the viscosity of the magma, potentially producing an increase of several orders of magnitude during syn-eruptive ascent and leading therefore to explosive eruptions (Moitra et al., 2018; Arzilli et al., 2019).

Accurate estimation of magma decompression rates is therefore a priority for modern volcanology. A few estimates are available for both effusive and explosive eruptions involving magmas of different compositions and viscosities mainly at arc volcanoes, where several methods based on both geophysical and petrological approaches have been developed (e.g., seismicity, groundmass crystallization, reaction rims in hydrous crystals; Scandone and Malone, 1985; Rutherford and Hill, 1993; Geschwind and Rutherford, 1995). Geochronometers based on fast-diffusing elements in melt and crystals represent a promising technique for estimating decompression rates caused by syn-eruptive magma ascent rates (Lloyd et al., 2014, 2016; Giuffrida et al., 2018; Barth et al., 2019; Viccaro et al., 2021; Myers et al., 2021). In this regard, volatile diffusion along melt pockets partially enclosed within host crystals, called melt embayments or melt tubes (Humphreys et al., 2008; Lloyd et al., 2014), takes into account elements directly impacted by ascent-driven degassing dynamics, offering the opportunity to investigate timescales relevant to the syn-eruptive degassing process (from seconds to hours). This approach measures compositional gradients of volatile elements (H_2O, CO_2, and S) that are produced by diffusion from the inner part of the embayment to the outer melt in response to decompression-induced degassing; these gradients can be numerically modeled in order to retrieve timescales of diffusion.

This technique has been applied to arc volcanoes involving basaltic and silica-rich magmas (Liu et al., 2007; Humphreys et al., 2008; Lloyd et al., 2014; Moussallam et al., 2019; Myers et al., 2021), as well as to some historical eruptions at Kilauea volcano (Ferguson et al., 2016). However, although the hypothesis that intense explosive eruptions are correlated with rapid decompression rates finds general consensus in the scientific community, a true quantification of such relationship has yet to be properly addressed. To date, there is a need to investigate more cases of open-system, persistently active basaltic volcanoes, where ordinary Strombolian or effusive activity can suddenly turn into unusual and unexpected, highly explosive eruptions.

This study aims to quantify differences in decompression rates related to variable degrees of explosivity of basaltic eruptions by modeling volatile diffusion along melt embayments, taking Mt. Etna, one of the world's most active and best-monitored open-conduit volcanoes, as a case study. The recent activity of Mt. Etna is characterized by a wide spectrum of eruptive styles, from effusive up to violent ash-dominated lava fountains occurring during paroxysmal eruptions (Aiuppa et al., 2007; Cannata et al., 2018; Viccaro et al., 2019; Borzì et al., 2020; Giuffrida et al., 2021), as well as Subplinian and Plinian events occurred in historical times (Coltelli et al., 2000). Some recent episodes from the post-2011 activity were selected for this study mainly for the possibility of integrating petrological data with those coming from geophysical signals acquired by monitoring networks installed on the volcano. The selected eruptions in order of increasing explosive behavior are: 1) the flank eruption of December 24-27, 2018 (DEC 2018 hereinafter), which affected the upper eastern side of the volcanic edifice and was accompanied by intense seismic activity (Borzì et al., 2020), produced an 8-km-high (a.s.l.) eruptive column in the proximal area (Corradini et al., 2020), with a Mass Eruption Rate (MER) of 0.90×10^5 kg/s (inferred using the calculation of Mastin et al., 2009); 2) the lava fountaining episode occurred at the New South East Crater (NSEC) on February 19, 2013 (NSEC 2018 hereinafter), which is part of the intense 2011-2013 paroxysmal activity (Giuffrida and Viccaro, 2017) and produced a 6-12 km-high (a.s.l.) eruptive plume (Calvari et al., 2018), with MER of 1.72×10^5 kg/s (Freret-Lorgeril et al., 2018); 3) the paroxysmal eruption occurred at Voragine Crater (VOR) on December 3, 2015 (VOR 2015 hereinafter), which represents the most violent eruptive event at Mt. Etna over the last 20 years (Cannata et al., 2018), producing a 15-km-high (a.s.l.) eruptive column (Calvari et al., 2018) with MER of 1.45×10^6 kg/s.

The choice of a single volcano and episodes from the same eruptive cycle offers the advantage of reducing the number of variables affecting our modeling, with a fixed plumbing system geometry at depth and comparable physical and chemical conditions of the erupted magmas (e.g., composition, temperature, pressure, viscosity and – at least in part – volatile contents). This strategy allows us to better understand and quantify the relationships between decompression rate and eruptive styles.

2. Methods

Air-quenched tephra samples were collected in distal areas from the point of emission during the eruptions and represent the peak in the explosive activity. Samples were sieved with mesh smaller than 1 cm in order to remove clasts possibly affected by post-eruptive water loss (Lloyd et al., 2013). The fraction between 2 mm and 1 cm was crushed and picked, whereas the fraction smaller than 2 mm was sieved without crushing. Olivine crystals of 0.35 – 1.00 mm in length were hand-picked from the clasts under a binocular microscope, mounted individually using the Crystalbond 509 mounting adhesive, and polished with silicon carbide papers (P1200 and P2400) and diamond pastes (6 µm, 3 µm, 1 µm and ¼ µm) until melt embayments were exposed. Then, olivine crystals were removed from Crystalbond 509 and cleaned in acetone before Raman spectroscopy analyses. Finally, they were individually embedded in epoxy resin for electron microprobe analysis (EMPA).

A Renishaw inVia confocal Raman micro-spectrometer (Laboratoire Magmas et Volcans, University of Clermont-Auvergne, France) was used for measuring H_2O concentrations along melt embayments. The micro-spectrometer is equipped with a 532.1 ±0.3 nm diode laser (200 mW output power), a Peltier-cooled CCD detector of 1024×256 pixels, and a Leica DM 2500 M optical microscope with a motorized XYZ stage. The laser beam of about 5 mW power was focused at 2 μm under the sample surface using a 100× objective in high confocality setting (slit aperture of 20 μm). The spectra were recorded from ~100 to 1350 cm^{-1} (i.e., the spectral region of the alumino-silicate network vibrations) with acquisition time of 120 seconds and from ~2900 to 3800 cm^{-1} (i.e., the spectral region of the O-H vibrations) for 240 seconds using the WiRE^{TM} 4.2 software. Basaltic glasses with different water contents (0 to 2.28 wt.%; Schiavi et al., 2018, and references therein) were used for water quantification using the external calibration procedure (Schiavi et al., 2018) and were analyzed several times during each analytical session in order to correct for the influence of the delivered energy on the band intensities (see Supplementary material for the calibration line). Analytical precision measured on reference glasses was better than 5% relative. The estimated accuracy is about 15% relative. Profile compositions of H_2O were measured along the central part of the embayments, from the inner toward the mouth of the melt tubes, with a spacing between each spot on the order of 5-8 μm.

Major elements, S and Cl in embayments were measured at the Dipartimento di Scienze della Terra, University of Milan, using a JEOL JXA 8200 Superprobe equipped with five wavelength dispersive spectrometers (WDS), one energy dispersive spectrometer (EDS) and one cathodoluminescence detector. The radius of Rowland circle is 140 mm for spectrometers 1, 2 and 3, bearing LDE1, LDE2, LDEB, TAP, PET, and LiF crystals and 100 mm for spectrometers 4 and 5, bearing a PETH and a LIFH crystals. Analytical conditions of 5 μm beam at 15 kV accelerating voltage and ~5 nA beam current were used. Analytical precision for all measured elements is on the order of 5%.

A Tescan Vega-LMU scanning electron microscope was also used for collecting major elements in olivine at the Dipartimento di Scienze Biologiche, Geologiche e Ambientali of the University of Catania (Italy). The microscope is equipped with an EDAX Neptune XM4–60 EDS micro-analyzer using an EDS coupled with an EDAX WDS LEXS (low energy WDS) calibrated for light elements. Operating conditions were set at 20 kV accelerating voltage and ~2 nA beam current. Repeated analyses on SPI 02753-AB Serial KF certified standards (Fo-rich olivine) during the analytical runs provided precision for all measured elements of 3-5%. Accuracy is on the order of 5%.

3. Results

Juvenile fragments (sideromelane and tachylite), crystals and lithics constitute the components of the analyzed pyroclasts (Fig. 1a). Juvenile fragments are abundant in the lava fountaining episodes (66 and 90 vol% respectively for NSEC 2013 and VOR 2015; Fig. 1b-d), whereas the highest percentage of lithics (~50 vol%; Fig. 1e) was observed in DEC 2018 tephra. Crystals consist mainly of plagioclase and represent <5 vol%.

Three types of external morphologies were recognized in the juvenile fragments: spongy, fluidal, and blocky (cf. Pompilio et al., 2017). Both spongy and fluidal morphologies are present in sideromelane clasts of the NSEC 2013 and VOR 2015 eruptions, although spongy morphology is prevalent in VOR 2015 products. These types of clasts show irregular shapes and contain a large number of small spherical or elliptical coalesced vesicles (Fig. 1b). Fluidal morphology mainly characterizes sideromelane clasts of the NSEC 2013 and DEC 2018 products. Interconnected tubular vesicles are common and are responsible for the elongated shape of these clasts (Fig. 1c). The groundmass of both spongy and fluidal clasts is characterized by low crystallinity. Blocky morphologies are mainly observed in tachylite clasts, which are affected by randomly oriented cracks and have low vesicularity (Fig. 1d). Blocky clasts are generally more crystalline compared to spongy and fluidal clasts; microlites of plagioclase are predominant in blocky clasts.

Fifteen olivine crystals hosting melt-embayments were selected for this study: 5 from NSEC 2013 products, 6 from VOR 2015 products and 4 from DEC 2018 products. Olivines occur as subhedral crystals, with rounded edges in the rim portion where the analyzed embayments are located (Fig. 2). Visible portions of surrounding glasses show variable proportions of microcrysts and vesicles: NSEC 2013 and VOR 2015 glasses are more vesiculated and less crystallized than DEC 2018 glasses, and plagioclase microcrysts observed in VOR 2015 glasses are chiefly acicular or swallow-tailed (Fig. 1f-h). The examined melt-embayments are mostly tubular-shaped (Fig. 2a-c), but few samples display a more irregular shape (Fig. 2d). A vesicle on the open side of the tube evidences the occurrence of a bubble, which is a key condition to constrain the boundary condition at end of the melt tube in diffusion models. The size of the embayments ranges between 49 and 144 µm, with longer embayments more common in NSEC 2013 and VOR 2015 products than in DEC 2018.

The embayments are hosted in olivine crystals with core compositions ranging from Fo_{74} to Fo_{84}, whereas the olivine rims show a narrower range from Fo_{74} to Fo_{79}, with a higher average forsterite content for VOR 2015 samples, indicating the existence of compositional zoning (i.e., normal and reverse) from the core of the crystals to the rim. Post-entrapment crystallization (PEC) effects on major elements compositions are not considered, since volatiles in embayments are the main objects of interest in this study. Glasses in the studied embayments for the three eruptive episodes display similar major element compositions, which are also rather uniform throughout the embayments (Fig. 3; Table S1), whereas matrix glasses outside the host olivine show slightly more evolved compositions (Table S1).

Water concentration profiles measured using Raman spectroscopy show that the concentrations progressively decrease toward the opening of the embayment (Fig. 4a-c; Table S2). The embayment interior of the NSEC 2013 samples shows water concentrations in the range of 0.9-1.3 wt.%. Higher contents in the range of 1.1-1.7 wt.% characterize the VOR 2015 embayments, except for one sample with a lower concentration (~0.9 wt.%; Fig. 4b). Markedly lower concentrations (0.3-0.7 wt.%) were measured in the DEC 2018 embayments. For each eruptive episode, the highest H_2O contents were found in the longest embayments, indicating that diffusive volatile loss affected the shorter ones more extensively. The three eruptive episodes selected for this study differ in the shape of water gradients. The VOR 2015 embayments show slightly decreasing concentrations from the innermost portions toward the opening, while a steep gradient is observed in the last 30-40 μm before the bubble, where H_2O concentrations drop to ~0.2-0.5 wt.%. Less steep gradients are observed in the NSEC 2013 embayments starting from 50-70 μm from the opening. The DEC 2018 embayments also display gentle gradients, reaching contents of 0.1-0.3 wt.% at the mouth.

Sulfur measurements in the interior of the embayments show that VOR 2015 samples are characterized by slightly higher concentrations, on the order of 718-1300 ppm, than the NSEC 2013 products, with concentrations of 809-1150 ppm, except for one sample characterized by a very low S content (~153-260 ppm) (Fig. 4d-f; Table S1). Compared to NSEC 2013 and VOR 2015 samples, the DEC 2018 products have slightly lower S concentrations ranging from 660 to 885 ppm. Although the concentrations generally decrease toward the open side of the embayments, clear gradient profiles cannot be recognized in some of the analyzed samples.

No gradients are observed for Cl in the studied embayments (Fig. 4g-i; Table S1). NSEC 2013 and VOR 2015 display similar concentrations ranging from 906 to 1721 ppm, with an average value of 1400 ppm. The interior of the embayments from the DEC 2018 eruption is characterized by higher Cl concentrations, which range between 2030 and 2137 ppm.

No CO_2 data are available for the selected embayments from the recent activity at Mt. Etna. Therefore, the modeling is applied considering only the diffusion of H_2O and S.

4. Discussion

4.1 Definition of the initial and boundary conditions for the diffusion modeling

Open melt tubes are generally considered to be under continuous exchange with the external melt. However, slight differences in their compositions indicate that equilibrium between the embayments and the external melt was not completely attained. The equilibrium between the host olivines and the melt-embayments and surrounding melt was evaluated by plotting Mg# of melts versus Fo measured at the rim of the host crystals (Fig. 5); the equilibrium Fo calculated using either the $K_d{}^{\text{Mg-Fe}}{}_{\text{Ol-liq}} = 0.30$ (Roeder and Emslie, 1970) or the K_d predicted (0.27-0.28) using the model by Toplis (2005) are shown. The compositions of the embayment melts plot outside the equilibrium field, having lower Mg# than that predicted to be in equilibrium with Fo_{74-79}. Similarly, the composition of DEC 2018 matrix glasses is in disequilibrium with the Fo at the olivine rim. By contrast, the Mg# values of the matrix glasses in NSEC 2013 and VOR 2015 samples are in equilibrium with the Fo values measured at the olivine rims. This evidence suggests that crystallization of the host olivine at the interface with the NSEC 2013 and VOR 2015 embayments may have induced some modifications in melt compositions before the final ascent, as highlighted by a slight decrease in MgO in the inner part of the embayment of few samples. The low diffusivities of major elements prevent the restoration of equilibrium between the embayments and the external melt, producing thus the observed differences.

Thermodynamic modeling performed using rhyolite-MELTS software (Gualda et al., 2012) tracks the evolution of melt composition in melt inclusions from the same eruptive episodes (Zuccarello et al., 2021). The modeling indicates that the equilibrium between the observed Fo compositions at olivine rims and the surrounding melts occurs at 18-24 MPa, 43-77 MPa and 59-116 MPa for DEC 2018, NSEC 2013 and VOR 2015 samples, respectively. One way to test the accuracy of these constraints is to determine the saturation pressures of volatiles following the approach described in Lloyd et al. (2014). Specifically, S diffusivity is lower than H_2O diffusivity (Zhang et al., 2007), potentially preserving its initial concentrations in the embayments interior during syn-eruptive degassing in timescales of 10 to 20 minutes, as demonstrated by Lloyd et al. (2014). This is not expected during pre-eruptive degassing, which takes place several hours or days before the eruption, allowing to restore the equilibrium with the external melt. The developing of a combined H_2O-CO_2-S degassing modeling, derived from melt inclusion compositions (Fig. 6; Zuccarello et al., 2021), allowed us to constrain both initial volatile concentrations and initial pressures for the diffusion modeling, by considering H_2O as the intermediate component between the H_2O-S and H_2O-CO_2 degassing models. Assuming that the concentration of S measured in the interior of the embayment is representative of its original content before ascent, the associated H_2O value derived from the H_2O-S degassing path (Fig. 6a) can be adopted as the initial concentration for diffusion modeling (Lloyd et al., 2014). Then, the H_2O value inferred from the H_2O-S model is used to constrain the saturation pressure on the H_2O-CO_2 degassing path, which is modeled as a closed system with an initial fraction of gas already exsolved of 0.03 (Zuccarello et al., 2021), as defined using VolatileCalc (Newman and Lowenstern, 2002). This saturation pressure is therefore assumed as initial for the diffusion modeling. Sulfur degassing can be modeled through mass balance calculations as suggested by Spilliaert et al. (2006), who provide the calculation of bulk partition coefficients (*D*) of S as a function of decompression and melt evolution. The closed-system degassing for S (Fig. 6a) is simulated at each step of degassing by using the batch fraction equation with initial H_2O = 3.37 wt.% at 300 MPa, according to the H_2O-CO_2 degassing path (Fig. 6b; Zuccarello et al., 2021). Initial exsolution of S occurs at lower pressure (Spilliaert et al., 2006), and the closed-system degassing has been modeled starting from the highest S concentration measured in melt inclusions, 3065 ppm, at a pressure of 180 MPa, which is derived from H_2O-CO_2 modeling at a corresponding H_2O content of 2.9 wt.% (details are reported in the Supplementary material). Estimated initial S exsolution pressure and vapor/melt bulk partition coefficient D (which increases progressively from 1 to 60) are consistent with values defined for past eruptions at Mt. Etna (Spilliaert et al., 2006).

Saturation pressures derived through S degassing model are 80-96 MPa, 62-95 MPa and 95-108 MPa for DEC 2018, NSEC 2013 and VOR 2015, respectively. These values are rather consistent with those inferred from thermodynamic equilibrium between external glasses and olivine rims for NSEC 2013 and VOR 2015 and significantly greater for DEC 2018, similar to those estimated for NSEC 2013. We assume that DEC 2018 samples were in equilibrium with the surrounding melt before the final ascent, and that syn-eruptive matrix crystallization may have led to subsequent disequilibrium with greater effects on DEC 2018 (Fig. 5) than NSEC 2013 and VOR 2015 products, according with petrographic observations. Therefore, we choose to use as initial pressures those estimated from the volatile degassing model approach. The conversion of the inferred starting pressures to depths is performed by considering an average lithostatic density of 2700 kg/m^3, resulting in 0.2 km a.s.l. – 0.9 km b.s.l. and 0.9–1.2 km b.s.l. respectively for the NSEC 2013 and VOR 2015 eruptions. These depths are consistent with the sources estimated by strainmeters data, which recorded strain changes of the summit area during lava fountaining episodes caused by sources located at 0 and 1.5 km b.s.l., respectively, for the paroxysmal series occurred at NSEC during the 2011-2013 activity (Bonaccorso et al., 2013) and for the paroxysmal activity at VOR on 3-5 December 2015 (Bonaccorso and Calvari, 2017). Analogously to what was observed for the 2011-2013 activity at NSEC, even the source feeding the intrusion of DEC 2018 eruption was located at a depth of 0 km b.s.l. (Aloisi et al., 2020), in agreement with the constraints derived from the degassing model. The associated initial H_2O concentrations for NSEC 2013, VOR 2015 and DEC 2018 embayments are constrained respectively in the range of 1.88–2.25 wt.%, 2.28–2.41 wt.% and 2.11–2.29 wt.%.

Diffusion coefficient is a critical parameter that strongly influences the modeling. Estimation of diffusion coefficient is based on the Arrhenius law and is chiefly a function of temperature, pressure, and melt compositions. For magmas of mafic to intermediate composition, pressure has a minor influence on H_2O diffusivity and can be neglected. Thus, H_2O diffusivity is estimated following the equation defined experimentally by Zhang et al. (2007):

$$D_{H_2O} = C_{H_2O} exp\left(-8.56 - \frac{19110}{T}\right) \quad [1]$$

where C_{H2O} is the concentration of water in wt.%, D_{H2O} the water diffusion coefficient in m^2/s and T the temperature in K. This equation was developed for basaltic melts, but the influence of variations in melt compositions on D_{H2O} is not considered. The effect of melt compositions on D_{H2O} can be parametrized as a function of the NBO/T ratio (Lloyd et al., 2014). The embayments investigated in this study display uniform major element compositions, so an average value of NBO/T can be considered for the H_2O diffusivity correction. We used the method described in Prata et al. (2019) in assigning cations to the role of T and for the calculation of NBO/T, providing an average value of NBO/T ~0.53 ± 0.04 for the melt compositions of the studied embayments, which can be broadly assumed to be intermediate between basalts and more evolved terms such as andesites and trachytes. The parametrization (Fig. 7) was performed by defining two distinct linear relationships between NBO/T and LogD_{H2O} calculated using as end members a basaltic composition (NBO/T = 0.82; Zhang et al., 2007) and either andesitic (NBO/T = 0.26; Behrens et al., 2004) or trachytic compositions (NBO/T = 0.16; Freda et al. (2003). The two parametrizations were performed at T = 1080 °C and H_2O = 2.41 wt.%, being respectively the temperature used to run the diffusion modeling (see below) and the highest H_2O value used as initial concentration. Although different from Etnean melt compositions, the andesitic and trachytic terms are the most similar among those available in the literature that are useful for the parametrization. The resulting D_{H2O} for NBO/T = 0.53 (±0.04) is lower than the diffusivity calculated through the equation [1] by a factor of 0.25 (±0.04) and 0.52 (±0.04) in the case of basalt-andesite and basalt-trachyte parametrization, respectively. The same parametrization at lower H_2O concentrations provided the same value of the correction factor. Two distinct diffusion models have been therefore performed for each embayment, considering the correction of D_{H2O} parametrized as a function of either the andesitic or trachytic end-member, i.e. multiplying the equation [1] by 0.25 and 0.52 respectively.

Diffusivity of S is dependent not only on temperature and composition, but also on oxygen fugacity, which affects the speciation of sulfur in the melt. Indeed, changing from oxidizing to reducing conditions results in an increase of about 2.5 orders of magnitude in diffusivity (Zhang et al., 2007). Such a dependence makes it difficult to develop a general equation to define S diffusivity. However, based on experiments on Etna and Stromboli melts, D_S was defined for basaltic liquids at conditions of ~3 log units below the quartz-fayalite-magnetite (QFM) buffer, taking into account the dependence on H_2O concentration (Zhang et al., 2007 and references therein):

$$D_S = exp\left(-8.21 - \frac{27692 - 651.6C_{H_2O}}{T}\right) \quad [2]$$

Although experiments conditions are more reduced compared to that inferred for Etnean magma (QFM; Zuccarello et al., 2021), the equation [2] was used for calculating S diffusivity for Mt. Etna melts in absence of other experiments on more oxidized systems.

A one-dimensional diffusion has been used for modeling the concentration profiles. Initial volatile concentrations are assumed to be homogeneous throughout the embayments and during diffusion mass exchange is allowed only from the interior of the embayment to the bubble growing at its mouth. The concentration at the interface between the melt and the bubble at the embayment outlet varies as the volatile content in the surrounding melt changes, according to the pressure-dependent degassing model. In contrast, zero-flux is assumed in the interior of the embayment adjacent to the host olivine crystal, and no exchange with (or growth of) the host olivine is assumed. Measured H_2O concentrations in the matrix glasses surrounding the host crystals are 0.13-0.35 wt.% and have been used to constrain the final concentrations. The corresponding pressures of 1-2 MPa have been used as final conditions for diffusion simulations, assuming instantaneous magma cooling. The diffusion coefficient has been estimated at isothermal conditions during the ascent with a temperature of 1080 °C (±10 °C). This corresponds to the average value constrained by thermodynamic simulations for melts of similar compositions to those measured in the embayments (Zuccarello et al., 2021), which is also consistent with the temperature of Mt. Etna lavas measured at the vent (Calvari et al., 1994). Thus, decompression rate (*dP/dt*) is the only free parameter allowed to change in the diffusion model, with the goal of identifying the value of decompression rate that minimizes the misfit with the measured H_2O concentrations in the embayment. During decompression, the volatile concentration at the embayment outlet changes as a function of the solubility and the pressure calculated at each step of the simulation. Therefore, variations in *dP/dt* affect the shape of the modeled gradients for same initial conditions. Simulations have been performed through a script code in Python language by changing progressively *dP/dt* within a defined range. Since gradients and diffusivity are better characterized for H_2O than for S, the best fit is determined by minimizing the χ^2 for H_2O modeling as follows:

$$\chi^2 = \sum_{i=1}^{n} \frac{(C_i - y_i)^2}{{\sigma_i}^2} \quad [3]$$

where C_i is the measured H_2O concentration at i position in the compositional profile, y_i is the modeled concentration and σ_i is the uncertainty associated to the measured concentration (estimated at 8% relative by Raman spectroscopy). Major sources of error are represented by uncertainties in estimated T, correction factors for the calculation of D_{H2O}, and initial H_2O concentrations constrained by the degassing model. A Monte Carlo approach has been employed in order to evaluate the uncertainty for each modeling by running one thousand up to ten thousand simulations, where these parameters have been randomly set within the estimated uncertainties assuming a normal distribution around the constrained central value ($2\sigma_T = \pm 10$ °C, $2\sigma_{\text{corr. factor}} = \pm 0.04$, $2\sigma_{H2Oi} = \pm 0.25$ wt.%). The accuracy associated to the equation [1] determined by Zhang et al. (2007) has not been included in the error evaluation since it would systematically affect each decompression rate estimation of the same factor (~3.5-4 in terms of MPa/s). The approach described above estimates a constant decompression rate for each compositional profile modeled in the embayments, assuming that decompression is only driven by magma ascent through the conduit. The conversion to decompression rate is justified by the presence of the bubble at the embayment mouth, presumably throughout the magma ascent, given that heterogeneous bubble nucleation requires very low supersaturation pressures (Shea, 2017). In natural systems, it is reasonable that the decompression rate from the reservoir to the surface is not constant due to the steep, nonlinear pressure gradients linked with magma vesiculation and fragmentation (Myers et a., 2021), so the estimates provided by diffusion modeling can be considered as integrated average values recorded by each embayment investigated in this study. For each modeling, the associated timescale t is calculated as:

$$t = \frac{P_i - P_f}{dP/dt} \qquad [4]$$

where P_i and P_f are the initial and final pressures and dP/dt is the corresponding decompression rate. The conversion into ascent velocity is calculated as:

$$v = \frac{1}{t}\left(\frac{P_i - P_f}{\rho g}\right) \qquad [5]$$

where ρ is the average lithostatic density and g is the gravitational acceleration (9.81 m/s^2).

4.2 Relationships between magma decompression rates and explosivity

Microanalyses along olivine-hosted melt embayments highlight H_2O concentration gradients in all the analyzed samples. Many samples display irregular concentration gradients for S, so that only those suitable for diffusion modeling were selected. The results of the volatile diffusion modeling are concordant with the expected increase in decompression rates as the explosivity of eruptions increases, where the highest decompression rates have been calculated for the VOR 2015 eruption (Fig. 8; Table 1). Modeling performed by using the correction factor of 0.25 yielded decompression rates of 0.28-0.44 MPa/s for VOR 2015 eruption (average ~0.36 ± 0.09 MPa/s), 0.09-0.20 MPa/s for NSEC 2013 eruption (~0.14 ± 0.10 MPa/s) and 0.016-0.071 MPa/s for DEC 2018 eruption (~0.045 ± 0.024 MPa/s). Two outliers are represented by the samples NSEC_EMB3 and VOR_EMB2, with decompression rates of 0.35 ± 0.06 MPa/s and 0.039 ± 0.008 MPa/s respectively. Considering the correction factor of 0.52, we obtained decompression rates of 0.55-0.92 MPa/s for VOR 2015 eruption (~0.76 ± 0.18 MPa/s), 0.18-0.41 MPa/s for NSEC 2013 eruption (~0.29 ± 0.10 MPa/s) and 0.035-0.150 MPa/s for DEC 2018 eruption (~0.094 ± 0.051 MPa/s), where the same outliers from NSEC 2013 and VOR 2015 produced respectively 0.72 ± 0.10 MPa/s and 0.080 ± 0.010 MPa/s. Excluding the outliers, the associated total ascent times range from 1.7 to 6.9 minutes for VOR 2015, from 3.8 to 13.8 minutes for NSEC 2013 and from 9.8 to 83.3 minutes for DEC 2018 eruption. The deviation of the NSEC 2013 outlier from other embayments of the same sample can be attributed to a greater effect of bubble expansion at the mouth of a small embayment in producing an apparently higher decompression rate. The longer time estimated for one sample of VOR 2015 eruption (20-40 minutes) could be related to a portion of magma ascending at a lower rate during the increase in Strombolian activity before the paroxysmal phase, and then being incorporated into the main flow. Such inference is consistent with the timing of the infrasonic early warning detected 30 minutes before the onset of the paroxysmal phase during the VOR 2015 episode (Ripepe et al., 2018). Alternatively, this olivine crystal could have been incorporated in the slowly ascending portion of the multiphase flow in contact with the wall of the conduit, where greater cooling and crystallization may lead to increased viscosity (Taddeucci et al., 2004). Estimated χ^2 values (Table 1) suggest good fits for the H_2O modeling (Fig. 9), considering the significance level at 5% and the degree of freedom (DF) calculated as: DF = $N_D - 1$, where N_D is the number of data points of the modeled embayment. A few samples are characterized by relatively high χ^2, possibly due to variation in decompression rate that affects natural samples (e.g., the VOR 2015 outlier) or because of slightly irregular H_2O gradients in samples with either a narrow tube neck or a wider mouth opening at the end of the tube, which, coupled with the effect of bubble expansion, can lead to an over-steepening of the H_2O profile predicted by one-dimensional numerical approaches. Therefore, diffusivity is strongly dependent on the embayment shape (deGraffenried and Shea, 2020) and more reliable results from one dimensional diffusion are obtained for tubular-shaped embayments. Concerning S profiles, too high χ^2 values resulted from modeling S diffusion at the same decompression rates estimated for H_2O diffusion, so they cannot be used to determine the goodness of fitting (χ^2 >1000).

The results obtained by modeling volatile diffusion in the embayments are overall consistent with the rates previously estimated for eruptions of comparable explosivity (e.g., Lloyd et al., 2014; Ferguson et al., 2016; Giuffrida et al., 2018). Ascent velocities estimated in this study for the intense NSEC 2013 and VOR 2015 eruptions at Mt. Etna are within the range obtained by Li diffusion modeling on plagioclase for some lava fountaining episodes from the 2011-2013 paroxysmal series at NSEC (4 – 64 m/s; Giuffrida et al., 2018). In addition, volatile diffusion modeling in embayments from the highly explosive 1974 eruption at Volcan de Fuego (Lloyd et al., 2014) and from the

Keanakakoi Layer 6 (Kilauea; c. 1650 CE; Ferguson et al., 2016) provided decompression rates of 0.32 – 0.47 MPa/s and ~ 0.45 MPa/s, respectively, which are comparable with those obtained for the lava fountaining of VOR 2015 eruption (0.36 – 0.79 MPa/s). Finally, the maximum timescales of magma ascent calculated for the DEC 2018 eruption (up to 83 minutes) are consistent with the beginning of the seismic sequence which affected the flank of the volcanic edifice a couple of hours before the opening of the fracture (Alparone et al., 2020).

Concerning the lava fountain episodes, the slightly deeper overpressurization of the source feeding the lava fountain during the VOR 2015 eruption may constitute the driving force behind the higher decompression rates estimated for this eruption compared with the NSEC 2013 lava fountaining. On the other hand, the higher MER of VOR 2015 compared with NSEC 2013 (1.45×10^6 kg/s and 1.72×10^5 kg/s, respectively; Freret-Lorgeril et al., 2018) can be related to a larger conduit radius of the VOR than the NSEC, whose respective values of 3.4 m and 1.6 m were calculated by taking into account the conservation of mass, expressed as $Q = \rho u A$, where Q is the MER (kg/s), ρ is the density of the multiphase fluid composed of liquid and gas, u is the ascent velocity (m/s), and A is the cross-sectional conduit area (m^2). A larger conduit size should allow more efficient syn-eruptive outgassing, in turn leading to an increase in MER and decompression rate.

5. Concluding remarks and implications

Selected eruptive episodes from the recent, post-2011 activity at Mt. Etna characterized by different explosivity allowed us to get insights into kinetics of magma ascent, evaluating how differences in magma decompression rates influence the energy of eruptions at an open-conduit basaltic volcano. Results from volatile diffusion modeling have demonstrated that the degree of explosivity of eruptions fed by magmas with similar initial physical and chemical conditions is positively correlated with decompression rates. In this regard, the magma erupted during the DEC 2018 event produced low-energy explosive activity compared to the two lava fountaining episodes, because of lower magma decompression rates (~ 0.045-0.094 MPa/s) than those estimated for the powerful VOR 2015 (~ 0.36-0.76 MPa/s) and NSEC 2013 (~ 0.14-0.29 MPa/s) eruptions. These results are consistent with the more dehydrated features observed in the melt inclusions found in DEC 2018 products, where depleted H_2O concentrations were attributed to melt re-equilibration by diffusive water loss (Zuccarello et al., 2021). Significant dehydration can affect magmas under open-system degassing conditions during storage at pressures <200 MPa, where CO_2 flushing leads to simulate a closed-system degassing path. Here, we have shown that the final degree of dehydration is strongly dependent on the kinetics of syn-eruptive ascent to the surface. Indeed, high magma decompression rate enables part of the initial H_2O cargo (up to 4.0 wt.% in these products) to be retained, which coupled with changes in the rheological properties of the magma leads to an increase in gas overpressure. On the contrary, low magma decompression rates favor the escape of volatiles from the melt, inducing therefore more extensive water depletion in melt inclusions by diffusive loss.

Previous studies highlighted a prominent role of gas flushing from the deepest levels of the plumbing system as a major factor controlling explosive dynamics (Allard et al., 2005; Aiuppa et al., 2007; Moretti et al., 2018). In this regard, the collapsing foam model (Vergniolle and Jaupart, 1986) has been so far considered more appropriate for explaining the explosive activity at Mt. Etna. However, results obtained from volatile diffusion modeling also highlight an important contribution of syn-eruptive degassing and its kinetics in determining the degree of magma fragmentation (i.e., rise speed model; Parfitt and Wilson, 1995). This inference is also supported by the nature of erupted tephra, testified by the presence of highly vesiculated and microlite-poor sideromelane emitted during paroxysmal episodes. As inferred from the investigation of textural characteristics of tephra emitted during other explosive eruptions in the last decades (e.g., the 2000 AD paroxysmal series at the South East Crater; Polacci et al., 2006), a combination of both degassing models can therefore explain the dynamics of explosive eruptions at Mt. Etna, where fast syn-eruptive degassing has major effects during the peak of lava fountaining, enabling a more efficient magma fragmentation. This study also emphasizes how the ability of Mount Etna volcano in transferring magmas throughout the upper part of the plumbing system can change over rather limited timespans, even when the same basic and volatile-rich magmas are involved. The chance to degas the original high volatile load more or less efficiently, which is indeed related to variable decompression rates experienced during the final ascent, can have therefore significant influence on the ensuing eruptive behavior, with dramatic repercussions in terms of hazard associated.

Acknowledgements

Francesco Zuccarello acknowledges the PhD fellowship and two PhD research grants from the University of Catania. This work was also supported by the funding program PIACERI 2020-22 of the University of Catania, project PAROSSISMA, code 22722132140 (Principal Investigator M. Viccaro). The Authors are also thankful to Andrea Risplendente for his technical support during the EMP data acquisition at the University of Milan and to Alessandro Aiuppa and Sumit Chakraborty for their comments during the manuscript preparation. The editorial handling of Chiara Maria Petrone has been greatly appreciated, together with the helpful suggestions provided by Madeleine Humphreys, Tom Shea and other three anonymous reviewers.

References

Aiuppa, A., Moretti, R., Federico, C., Giudice, G., Liuzzo, M., Papale, P., Shinohara, H., Valenza, M., 2007. Forecasting Etna eruptions by real-time observation of volcanic gas composition. Geology, 35, 1115-1118. https://doi.org/10.1130/G24149A.1.

Allard, P., Burton, M., Mure, F., 2005. Spectroscopic evidence for a lava fountain driven by previously accumulated magmatic gas. Nature, 433, 407–410. https://doi.org/10.1038/nature03246.

Aloisi, M., Bonaccorso, A., Cannavò, F., Currenti, G., Gambino, S., 2020. The 24 December 2018 eruptive intrusion at Etna volcano as revealed by multidisciplinary continuous deformation networks (CGPS, borehole strainmeters and tiltmeters). J. Geophys. Res: Solid Earth, 125, e2019JB019117. https://doi.org/10.1029/2019JB019117.

Alparone, S., Barberi, G., Giampiccolo, E., Maiolino, V., Mostaccio, A., Musumeci, C., Scaltrito, A., Scarfì L., Tuvè, T., Ursino, A., 2020. Seismological constraints on the 2018 Mt. Etna (Italy) flank eruption and implications for the flank dynamics of the volcano. Terra Nova, 1–11. https://doi.org/10.1111/ter.12463.

Arzilli, F., La Spina, G., Burton, M.R., Polacci, M., Le Gall, N., Harteley, M.E., Di Genova, D., Cai, B., Vo, N.T., Bamber, E.C., Nonni, S., Atwood, R., Llewellin, E.W., Brooker, R.A., Mader, H.M., Lee, P.D., 2019. Magma fragmentation in highly explosive basaltic eruptions induced by rapid crystallization. Nat. Geosci., 12, 1023–1028. https://doi.org/10.1038/s41561-019-0468-6.

Barth, A., Newcombe, M.E., Plank, T., Gonnermann, H., Hajimirza, S., Soto, G.J., Saballos, A., Hauri, E., 2019. Magma decompression rate correlates with explosivity at basaltic volcanoes - constraints from water diffusion in olivine. J. Volcanol. Geotherm. Res., 387, 106664. https://doi.org/10.1016/j.jvolgeores.2019.106664.

Behrens, H., Zhang, Y., Xu, Z., 2004. H_2O diffusion in dacitic and andesitic melts. Geochim. Cosmochim. Acta 68, 5139–5150. https://doi.org/10.1016/j.gca.2004.07.008.

Bonaccorso, A., Currenti, G., Linde, A., Sacks, S., 2013. New data from borehole strainmeters to infer lava fountain sources (Etna 2011–2012). Geophys. Res. Lett., 40 (14), 3579–3584. https://doi.org/10.1002/grl.50692.

Bonaccorso, A., Calvari, S., 2017. A new approach to investigate an eruptive paroxysmal sequence using camera and strainmeter networks: Lessons from the 3–5 December 2015 activity at Etna volcano. Earth Planet. Sci. Lett., 475, 231–241. https://doi.org/10.1016/j.epsl.2017.07.020.

Borzi, A.M., Giuffrida, M., Zuccarello, F., Palano, M., Viccaro, M., 2020. The Christmas 2018 eruption at Mount Etna: Enlightening how the volcano factory works through a multiparametric inspection. Geochem. Geophys. Geosyst., 21, e2020GC009226. https://doi.org/10.1029/2020GC009226.

Calvari, S., Coltelli, M., Neri, M., Pompilio, M., Scribano, V., 1994. The 1991-1993 Etna eruption: chronology and lava flow-field evolution. Acta Vulcanol., 4, 1–14.

Calvari, S., Cannavò, F., Bonaccorso, A., Spampinato, L., Pellegrino, A.G., 2018. Paroxysmal Explosions, Lava Fountains and Ash Plumes at Etna Volcano: Eruptive Processes and Hazard Implications. Front. Earth Sci., 2018, 6, 107. https://doi.org/10.3389/feart.2018.00107.

Cannata, A., Di Grazia, G., Giuffrida, M., Gresta, S., Palano, M., Sciotto, M., Viccaro, M. Zuccarello, F., 2018. Space-time evolution of magma storage and transfer at Mt. Etna volcano (Italy): The 2015–2016 reawakening of Voragine crater. Geochem. Geophys. Geosyst., 19, 471–495. https://doi.org/10.1002/2017GC007296.

Coltelli, M., Del Carlo, P., Vezzoli, L., 2000. Stratigraphic constraints for explosive activity in the past 100 ka at Etna Volcano, Italy. Int. J. Earth Sci., 89, 665–677. https://doi.org/10.1007/s005310000117.

Corradini, S., Guerrieri, L., Stelitano, D., Salerno, G., Scollo, S., Merucci, L., Prestifilippo, M., Musacchio, M., Silvestri, M., Lombardo, V., Caltabiano, T., 2020. Near real-time monitoring of the Christmas 2018 Etna eruption using SEVIRI and products validation. Rem. Sens., 12 (8), 1336. https://doi.org/10.3390/rs12081336.

deGraffenried R., Shea, T., 2020. Modeling diffusion in 1D within melt embayments: correcting for 3D geometry. AGU Fall Meeting 2020.

Ferguson, D.J., Gonnermann, H.M., Ruprecht, P., Plank, T., Hauri, E.H., Houghton, B.F., Swanson, D.A., 2016. Magma decompression rates during explosive eruptions of Kilauea volcano, Hawaii, recorded by melt embayments. Bull. Volcanol., 78 (10). https://doi.org/10.1007/s00445-016-1064-x.

Freda, C., Baker, D. R., Romano, C., Scarlato, P., 2003. Water diffusion in natural potassic melts. Geol. Soc. Spec. Publ., 213, 53–62. https://doi.org/10.1144/GSL.SP.2003.213.01.04.

Freret-Lorgeril, V., Donnadieu, F., Scollo, S., Provost, A., Fréville, P., Guéhenneux, Y., Hervier, C., Prestifilippo, M., Coltelli, M., 2018. Mass Eruption Rates of Tephra Plumes During the 2011–2015 Lava Fountain Paroxysms at Mt. Etna From Doppler Radar Retrievals. Front. Earth Sci., 6-73. https://doi.org/10.3389/feart.2018.00073.

Geschwind, C.-H., Rutherford, M.J., 1995. Crystallization of microlites during magma ascent: the fluid mechanics of 1980-86 eruptions at Mount St. Helens. Bull. Volcanol., 57,356-370. https://doi.org/10.1007/BF00301293.

Giuffrida, M., Viccaro, M., 2017. Three years (2011–2013) of eruptive activity at Mt. Etna: Working modes and timescales of the modern volcano plumbing system from micro-analytical studies of crystals. Earth Sci. Rev., 171, 289–322. https://doi.org/10.1016/j.earscirev.2017.06.003.

Giuffrida, M., Viccaro, M. Ottolini, L., 2018. Ultrafast syn-eruptive degassing and ascent trigger high-energy basic eruptions. Sci. Rep., 8, 147. https://doi.org/10.1038/s41598-017-18580-8.

Giuffrida, G., Scandura, M., Costa, G., Zuccarello, F., Sciotto, M., Cannata, A., Viccaro, M., 2021. Tracking the summit activity of Mt. Etna volcano between July 2019 and January 2020 by integrating petrological and geophysical data. J. Volcanol. Geotherm. Res., 418, article 107350. https://doi.org/10.1016/j.jvolgeores.2021.107350.

Gonnermann, H.M., Manga, M., 2007. The fluid mechanics of volcanic eruptions. Annu. Rev. Fluid Mech. 39, 321–356. https://doi.org/10.1146/annurev.fluid.39.050905.110207.

Gualda, G.A.R., Ghiorso, M.S., Lemons, R. and Carley, T.L., 2012. Rhyolite-MELTS: a modified calibration of MELTS optimized for silica-rich, fluid-bearing magmatic systems. J. Petrol., 53, 875–890. https://doi.org/10.1093/petrology/egr080.

Houghton, B.F., Wilson, C.J.N., Del Carlo, P., Coltelli, M., Sable, J.E., Carey, R.J., 2004. The influence of conduit processes on changes in style of basaltic Plinian eruptions: Tarawera 1886 and Etna 122 BC. J. Volcanol. Geotherm. Res. 137, 1–14. https://doi.org/10.1016/j.jvolgeores.2004.05.009.

Humphreys, M.C.S., Menand, T., Blundy, J.D., Klimm, K., 2008. Magma ascent rates inexplosive eruptions: Constraints from H_2O diffusion in melt inclusions. Earth Planet. Sci. Lett., 270 (1-2), 25-40. https://doi.org/10.1016/j.epsl.2008.02.041.

La Spina, G., Arzilli, F., Llewellin, E.W., Burton, M.K., Clarke, A.B., de' Michieli Vitturi, M., Polacci, M., Hartley, M.E., Di Genova, D., Mader, H.M, 2021. Explosivity of basaltic lava fountains is controlled by magma rheology, ascent rate and outgassing. Earth Planet. Sci. Lett., 553, 116658. https://doi.org/10.1016/j.epsl.2020.116658.

Liu, Y., Anderson, A.T., Wilson, C.J.N., 2007. Melt pockets in phenocrysts and decompression rates of silicic magmas before fragmentation. J. Geophys. Res. Solid Earth, 112 (B6), 12. https://doi.org/10.1029/2006JB004500.

Lloyd, A., Ruprecht, P., Hauri, E., Rose, W., Gonnermann, H.H., Plank, T., 2014. NanoSIMS results from olivine-hosted melt embayments: Magma ascent rate during explosive basaltic eruptions. J. Volcanol. Geotherm. Res., 283, 1–18. https://doi.org/10.1016/j.jvolgeores.2014.06.002.

Lloyd, A.S., Ferriss, E., Ruprecht, P., Hauri, E., Brian, R.J., Plank, T., 2016. An assessment of clinopyroxene as a recorder of magmatic water and magma ascent rate. J. Petrol., 57(10), 1865-1886. https://doi.org/10.1093/petrology/egw058.

Mastin, L. G., Guffanti, M., Servranckx, R., Webley, P., Barsotti, S., Dean, K., Durant, A., Ewert, W., Neri, A., Rose, W. I., Schneider, D., Siebert, L., Stunder, B., Swanson, G., Tupper, A., Volentik, A., and Waythomas, C. F., 2009. A multidisciplinary effort to assign realistic source

parameters to models of volcanic ash-cloud transport and dispersion during eruptions. J. Volcan. Geoth. Res., 186, 10–21. https://doi.org/10.1016/j.jvolgeores.2009.10.013.
Mangan, M.T., Cashman, K.V., 1996. The structure of basaltic scoria and reticulite and inferences for vesiculation, foam formation, and fragmentation in lava fountains. J. Volcanol. Geotherm. Res., 73, 1–18. https://doi.org/10.1016/0377-0273(96)00018-2.
Moitra, P., Gonnermann, H. M., Houghton, B. F., Tiwary, C. S., 2018. Fragmentation and Plinian eruption of crystallizing basaltic magma. Earth Planet. Sci. Lett., 500, 97–104. https://doi.org/10.1016/j.epsl.2018.08.003.
Moretti, R., Métrich, N., Arienzo, I., Di Renzo, V., Aiuppa, A., Allard, P., 2018. Degassing vs. eruptive styles at Mt. Etna volcano (Sicily, Italy). Part I: Volatile stocking, gas fluxing, and the shift from low-energy to highly explosive basaltic eruptions. Chem. Geol., 482, 1-17. https://doi.org/10.1016/j.chemgeo.2017.09.017.
Moussallam, Y., Rose-Koga, E. F., Koga, K. T., Médard, E., Bani, P., Devidal, J.-L., Tari, D., 2019. Fast ascent rate during the 2017–2018 Plinian eruption of Ambae (Aoba) volcano: A petrological investigation. Contrib. Mineral. Petrol., 174, 90. https://doi.org/10.1007/s00410-019-1625-z.
Mourtada-Bonnefoi C.C., Laporte D., 2004. Kinetics of bubble nucleation in a rhyolitic melt: an experimental study of the effect of ascent rate. Earth Planet. Sci. Lett., 218, 521-537. https://doi.org/10.1016/S0012-821X(03)00684-8.
Myers M.L., Druitt T.H., Schiavi F., Gurioli L., Flaherty T., 2021. Evolution of magma decompression and discharge during a Plinian event (Late Bronze-Age eruption, Santorini) from multiple eruption-intensity proxies. Bull. Volcanol., 83, 3. https://doi.org/10.1007/s00445-021-01438-3.
Newman, S., Lowenstern, J.B., 2002. VolatileCalc: a silicate melt–H_2O–CO_2 solution model written in Visual Basic for excel. Comput. Geosci., 28, 597–604. https://doi.org/10.1016/S0098-3004(01)00081-4.
Parfitt, E.A., Wilson, L., 1995. Explosive volcanic eruptions IX: The transition between Hawaiian-style lava fountaining and Strombolian explosive activity. Geophys. J. Int., 121, 226–232. https://doi.org/10.1111/j.1365-246X.1995.tb03523.x.
Pérez, W., Freundt, A., Kutterolf, S., Schmincke, H.U., 2009. The Masaya Triple Layer: A 2100 year old basaltic multi-episodic Plinian eruption from the Masaya Caldera Complex (Nicaragua). J. Volcanol. Geotherm. Res., 179 (3-4), 191-205. https://doi.org/10.1016/j.jvolgeores.2008.10.015.

Polacci, M., Corsaro, R.A., Andronico, D., 2006. Coupled textural and compositional characterization of basaltic scoria: Insights into the transition from Strombolian to fire fountain activity at Mount Etna, Italy. Geology, 34 (3), 201–204. https://doi.org/10.1130/G22318.1.

Pompilio, M., Bertagnini, A., Del Carlo, P., Di Roberto, A., 2017. Magma dynamics within a basaltic conduit revealed by textural and compositional features of erupted ash: the December 2015 Mt. Etna paroxysms. Sci. Rep., 7, 4805. https://doi.org/10.1038/s41598-017-05065-x.

Ripepe, M., Marchetti, E., Delle Donne, D., Genco, R., Innocenti, L., Lacanna, G., Valade, S., 2018. Infrasonic early warning system for explosive eruptions. J. Geophys. Res. Solid Earth, 123, 9570–9585. https://doi.org/10.1029/2018JB015561.

Roeder, P.L., Emslie, R.F., 1970. Olivine-Liquid Equilibrium. Contr. Mineral. and Petrol. 29, 275-289. https://doi.org/10.1007/BF00371276.

Rutherford, M.J., Hill, P.M., 1993. Magma ascent rates from amphibole breakdown: Experiments and the 1980-1986 Mount St. Helens eruptions. J. Geophys. Res., 98, 19667-19685. https://doi.org/10.1029/93JB01613.

Rutherford, M. J., 2008. Magma ascent rates. Rev. Mineral. Geochem., 69, 241–271. https://doi.org/10.2138/rmg.2008.69.7.

Scandone, R.S., Malone, S., 1985. Magma supply, magma discharge and readjustment of the feeding system of Mount St. Helens during 1980. J. Volcanol. Geotherm. Res., 23, 239-262. https://doi.org/10.1016/0377-0273(85)90036-8.

Schiavi, F., Bolfan-Casanova, N., Withers, A.C., Médard, E., Laumonier, M., Laporte, D., Flaherty, T., Gómez-Ulla, A., 2018. Water quantification in silicate glasses by Raman spectroscopy: correcting for the effects of confocality, density and ferric iron. Chem. Geol., 483, 312–331. https://doi.org/10.1016/j.chemgeo.2018.02.036.

Shea, T., 2017. Bubble nucleation in magmas: A dominantly heterogeneous process? J. Volcanol Geotherm. Res., 343, 155-170.

Spilliaert, N., Allard, P., Métrich, N., Sobolev. A.V., 2006. Melt inclusion record of the conditions of ascent, degassing and extrusion of volatile-rich alkali basalt during the powerful 2002 flank eruption of Mount Etna (Italy). J. Geophys. Res., 111, B04203. https://doi.org/10.1029/2005JB003934.

Taddeucci, J., Pompilio, M., Scarlato, P., 2004. Conduit processes during the July-August 2001 explosive activity of Mt. Etna (Italy): Inferences from glass chemistry and crystal size distribution of ash particles. J. Volcanol Geotherm. Res., 137, 33–54, https://doi.org/10.1016/j.jvolgeores.2004.05.011.

Toplis, M.J., 2005. The thermodynamics of iron and magnesium partitioning between olivine and liquid: criteria for assessing and predicting equilibrium in natural and experimental systems. Contrib. Mineral. Petrol., 149, 22–39. https://doi.org/10.1007/s00410-004-0629-4.

Vergniolle, S., Jaupart, C., 1986. Separated twophase flow and basaltic eruptions. J. Geophys. Res., 91, 12842–12860. https://doi.org/10.1029/JB091iB12p12842.

Viccaro, M., Giuffrida, M., Zuccarello, F., Scandura, M., Palano, M., Gresta, S., 2019. Violent paroxysmal activity drives self-feeding magma replenishment at Mt. Etna. Sci. Rep., 9, 6717, https://doi.org/10.1038/s41598-019-43211-9.

Viccaro, M., Cannata, A., Cannavò, F., De Rosa, R., Giuffrida, M., Nicotra, E., Petrelli, M., Sacco, G., 2021. Shallow conduit dynamics fuel the unexpected paroxysms of Stromboli volcano during the summer 2019. Sci. Rep. 11, 266. https://doi.org/10.1038/s41598-020-79558-7.

Walker, G.P.L., Self, S., Wilson, L., 1984. Tarawera 1886, New Zealand – a basaltic plinian fissure eruption. J. Volcanol. Geotherm. Res. 21, 61–78. https://doi.org/10.1016/0377-0273(84)90016-7.

Williams, S.N., 1983. Plinian airfall deposits of basaltic composition. Geology 11, 211–214. https://doi.org/10.1130/0091-7613(1983)11<211:PADOBC>2.0.CO;2.

Zhang, Y., Xu, Z., Zhu, M., Wang, H., 2007. Silicate melt properties and volcanic eruptions. Rev. Geophys., 72, 171–225. https://doi.org/10.1029/2006RG000216.

Zuccarello, F., Schiavi, F., Viccaro, M., 2021. Magma dehydration controls the energy of recent eruptions at Mt. Etna volcano. Terra Nova, 33, 423-429. https://doi.org/10.1111/ter.12527.

Figures

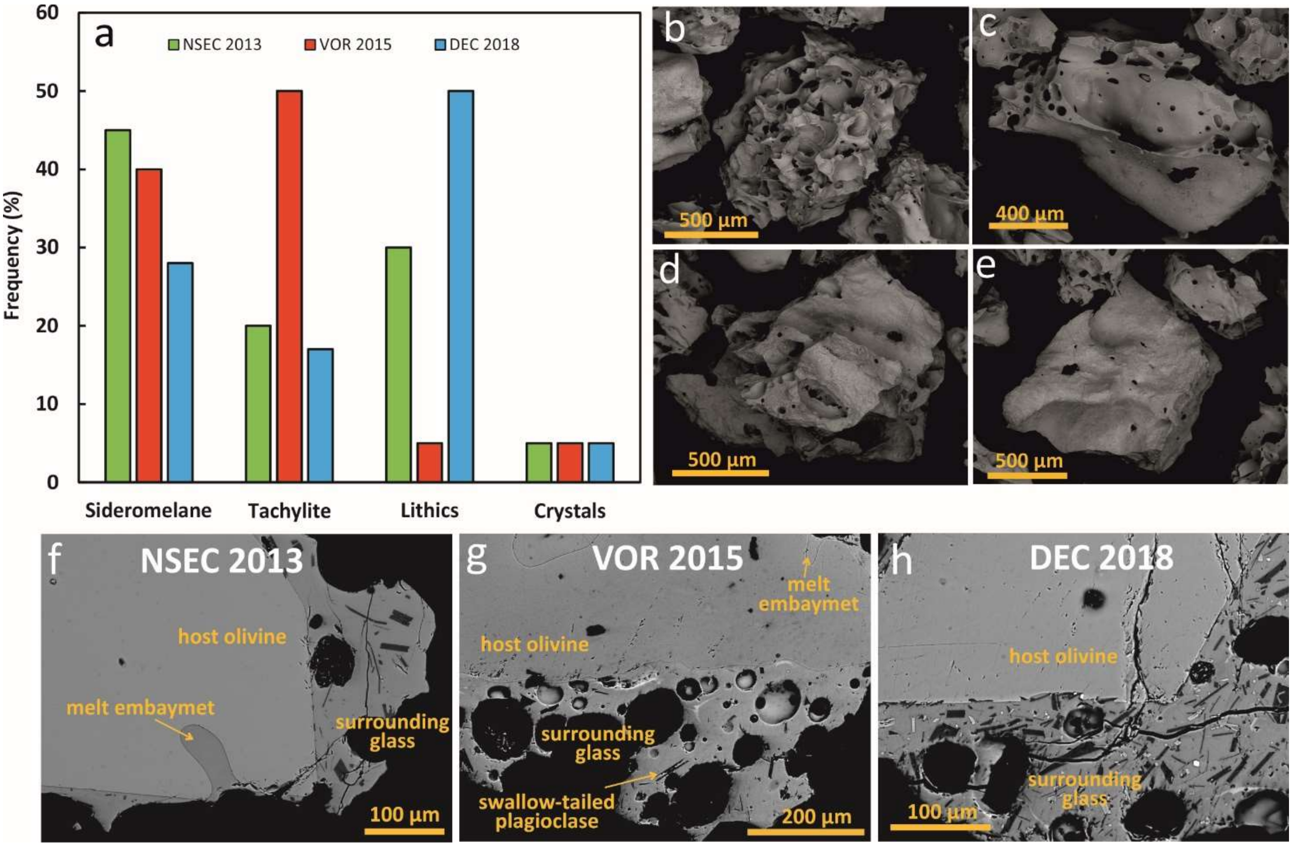

Figure 1. (a) Histograms showing the percentages of clasts found in tephra emitted during the selected eruptive episodes from the post-2011 activity, and BSE images showing: (b) sideromelane clast with spongy morphology; (c) sideromelane clast with fluidal morphology; (d) tachylite clast with blocky morphology; (e) lithic clast; (f) host-olivine and surrounding glass from NSEC 2013 samples; (g) host olivine and surrounding glass from VOR 2015 samples; (h) host-olivine and surrounding glass from DEC 2018 samples.

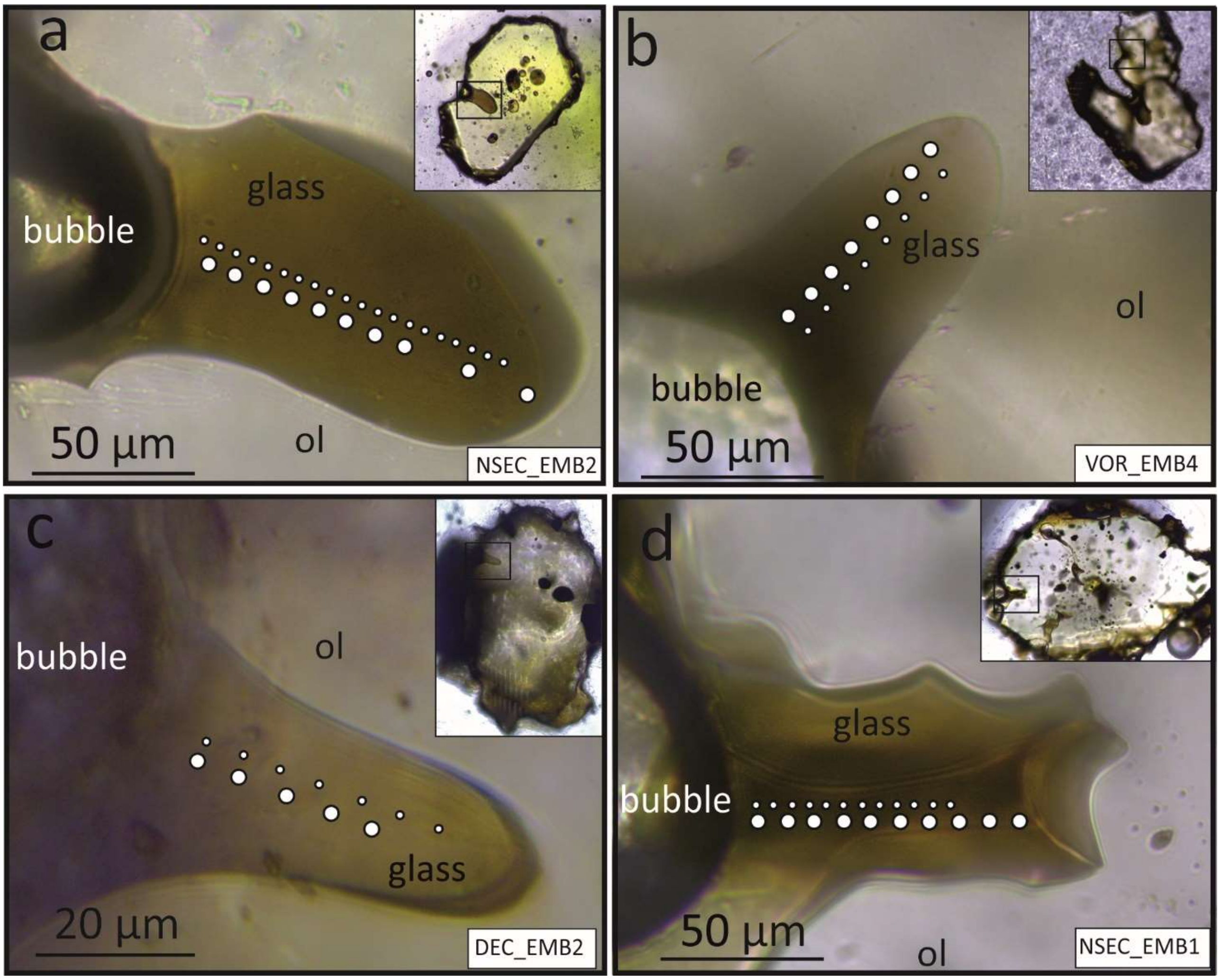

Figure 2. Images taken under optical microscope of representative melt-embayments analyzed using Raman spectroscopy (small white spots) and EMP (great white spots). Most of samples are tubular-shaped (a-c), few samples show more irregular shape (d). Inserts show the whole olivine crystals hosting melt embayments.

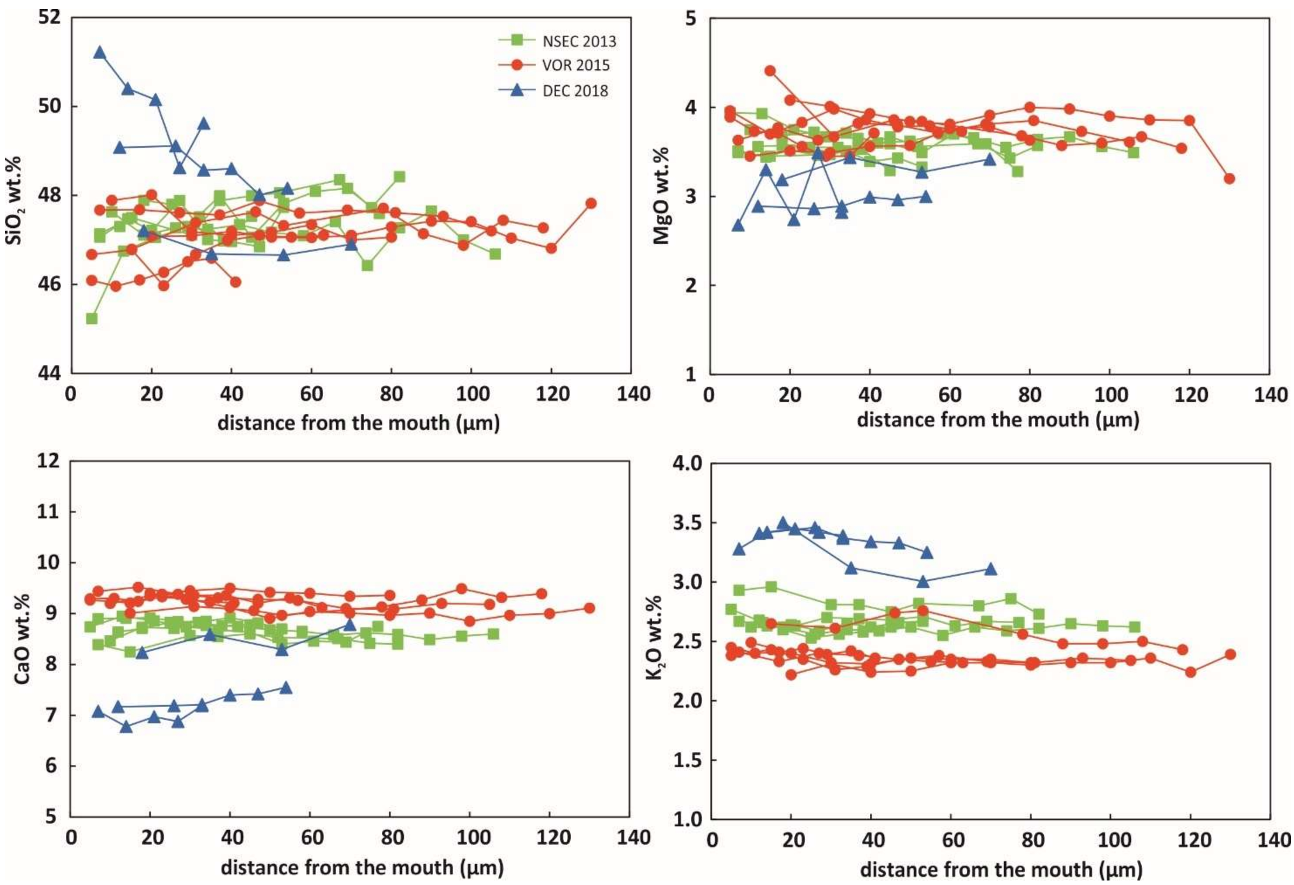

Figure 3. Selected major elements variations in melt-embayments found in products of the post-2011 activity at Mt. Etna as a function of the distance from the mouth of the embayment.

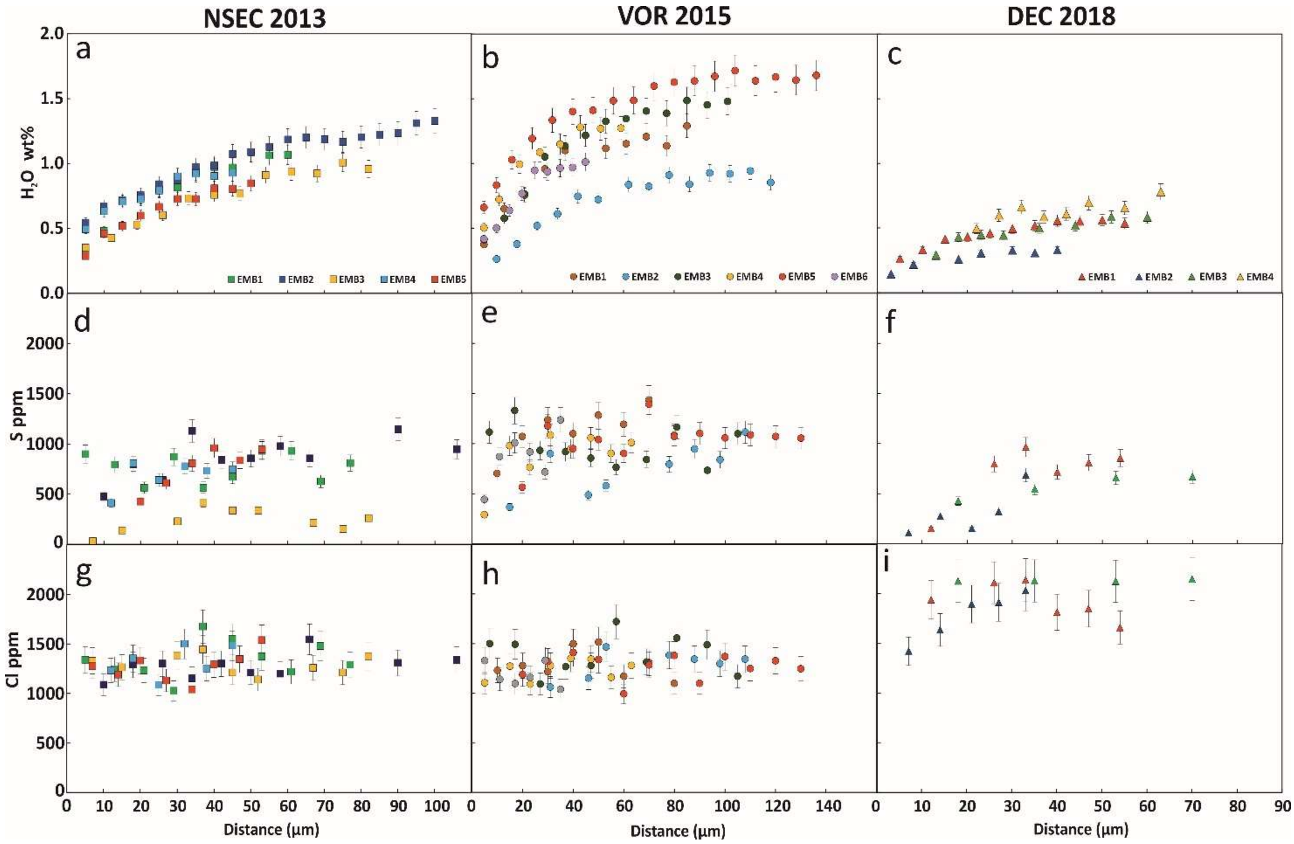

Figure 4. Compositional profiles for H_2O (a-c), S (d-f) and Cl (g-i) measured along each embayment of NSEC 2013 (a, d, g), VOR 2015 (b, e, h) and DEC 2018 (c, f, i) eruptions. S and Cl compositions in DEC2018_emb4 sample were collected by analyzing two spots in the embayment interior (see Table S2).

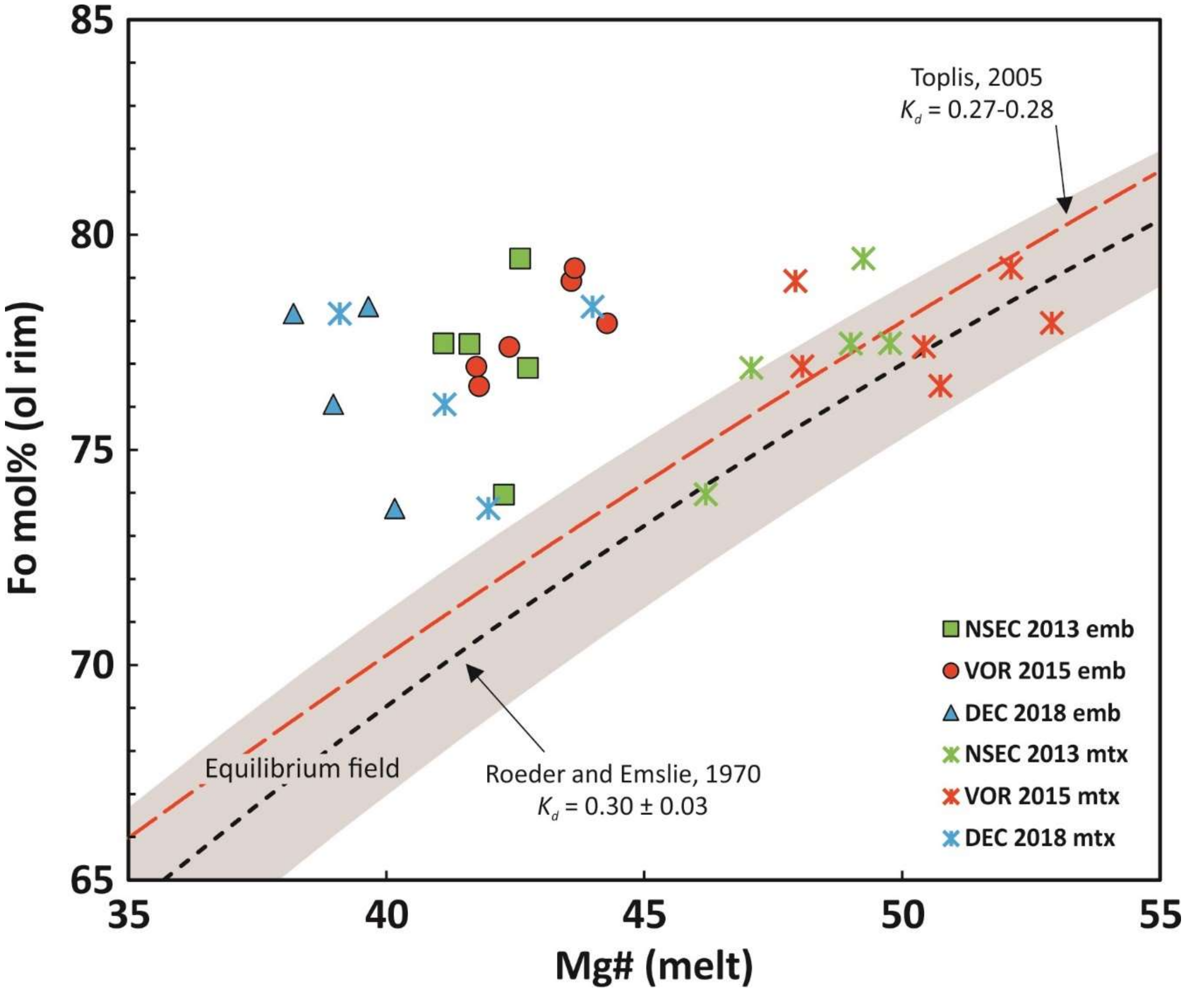

Figure 5. Diagrams showing the measured Fo mol% at the rim of host-olivine crystals vs. Mg# estimated in external melt (stars) and melt embayments for NSEC 2013 (green squares), VOR 2015 (red circles) and DEC 2018 (blue triangles). The equilibrium field (gray area) is calculated by using the $K_D^{\mathrm{ol(Mg/Fe)/melt(Mg/Fe)}} = 0.30 \pm 0.03$ (the dashed black line represents the central value) by Roeder and Emslie (1970), similar to K_D values predicted using the model by Toplis (2005) (dashed red line).

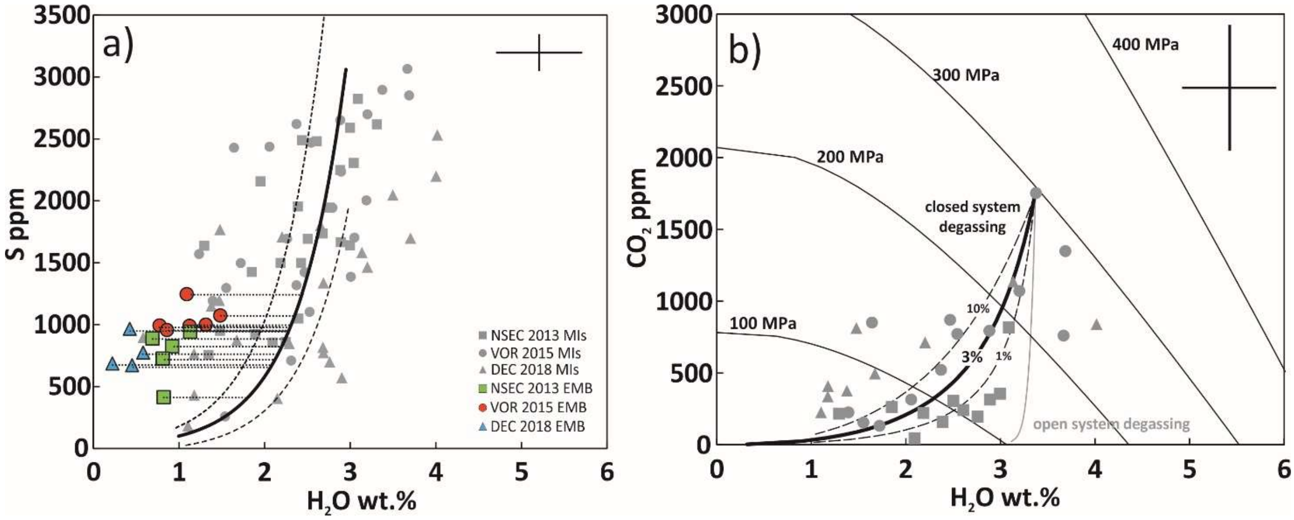

Figure 6. (a) Diagram reporting the average values of H_2O-S compositions in the interior of the embayments and the degassing model for the H_2O-S system on MIs from the same eruptive episodes (restored compositions for volatile loss; data from Zuccarello et al., 2021). Sulfur degassing has been modeled by using the mass balance approach described in Spilliaert et al. (2006) (See supplementary data for details). The thick black line is the best fit model, which is obtained starting from pressure of 180 MPa, S = 3065 ppm and H_2O = 2.9 wt.%, at melt fraction f = 85% and initial gas phase α_0 = 3%. Initial H_2O concentrations before diffusive loss during ascent can be inferred from S degassing, as well as the corresponding initial pressures are derived from the H_2O-CO_2 system. The dashed lines represent the $\pm 1\sigma$ of S degassing model, while the thin dotted lines indicate the potential initial H_2O contents for each embayment (green squares: NSEC 2013; red circles: VOR 2015; blue triangles: DEC 2018). (b) H_2O-CO_2 closed degassing model on MIs from the same eruptive episodes (Zuccarello et al., 2021). The thick black line is the intermediate path (with initial gas phase = 3%) used for constraining initial pressures in the diffusion modeling for each embayment.

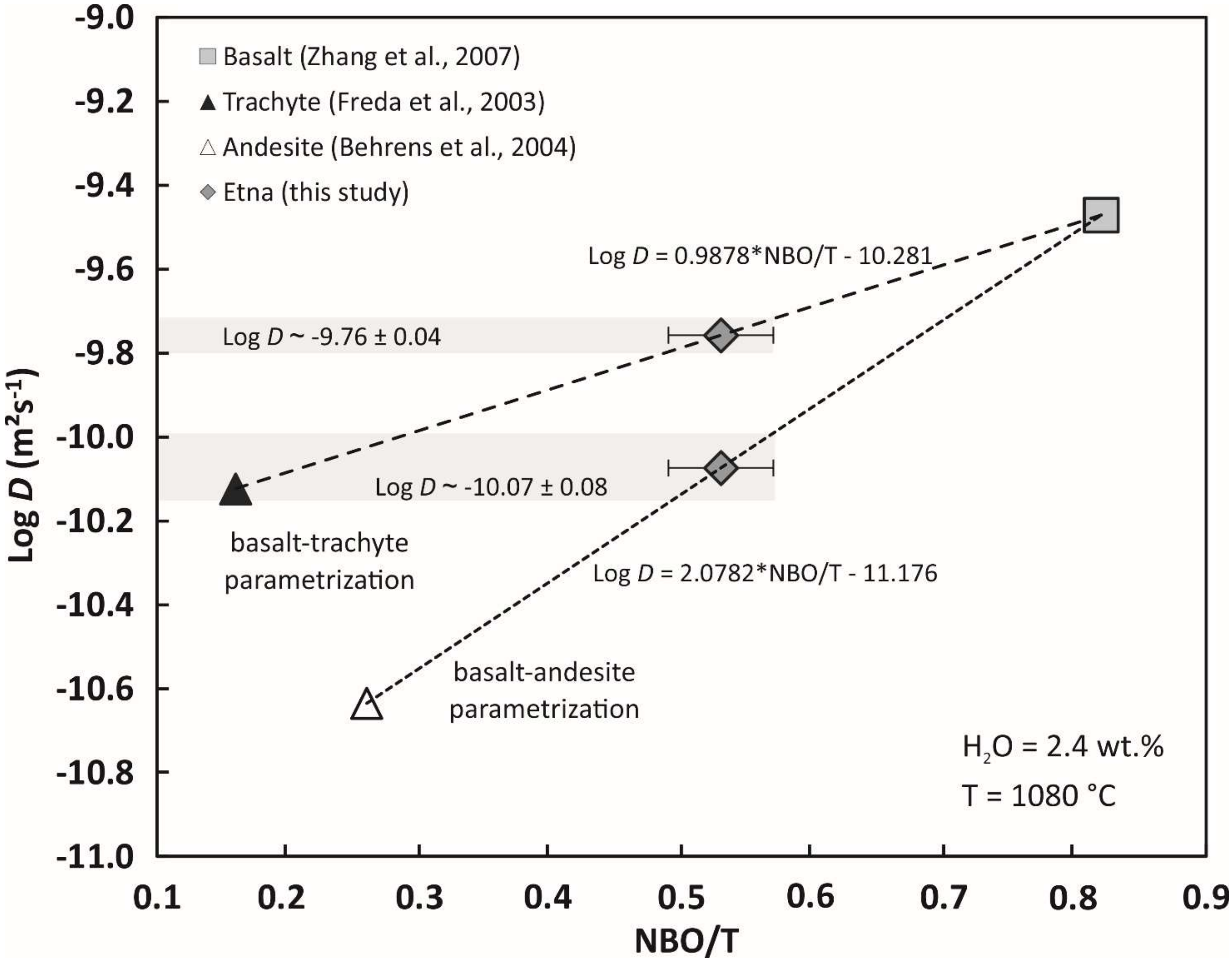

Figure 7. Parametrization on H_2O diffusivity (m^2/s) for Mt. Etna K-trachybasalt compositions, using a basalt from Zhang et al. (2007) and two different end members: an andesite from Behrens et al. (2004) and a trachyte from Freda et al. (2003). Two distinct linear relationships are defined at H_2O = 2.3 wt.% and T = 1080 °C between estimated Log$D$ and NBO/T values.

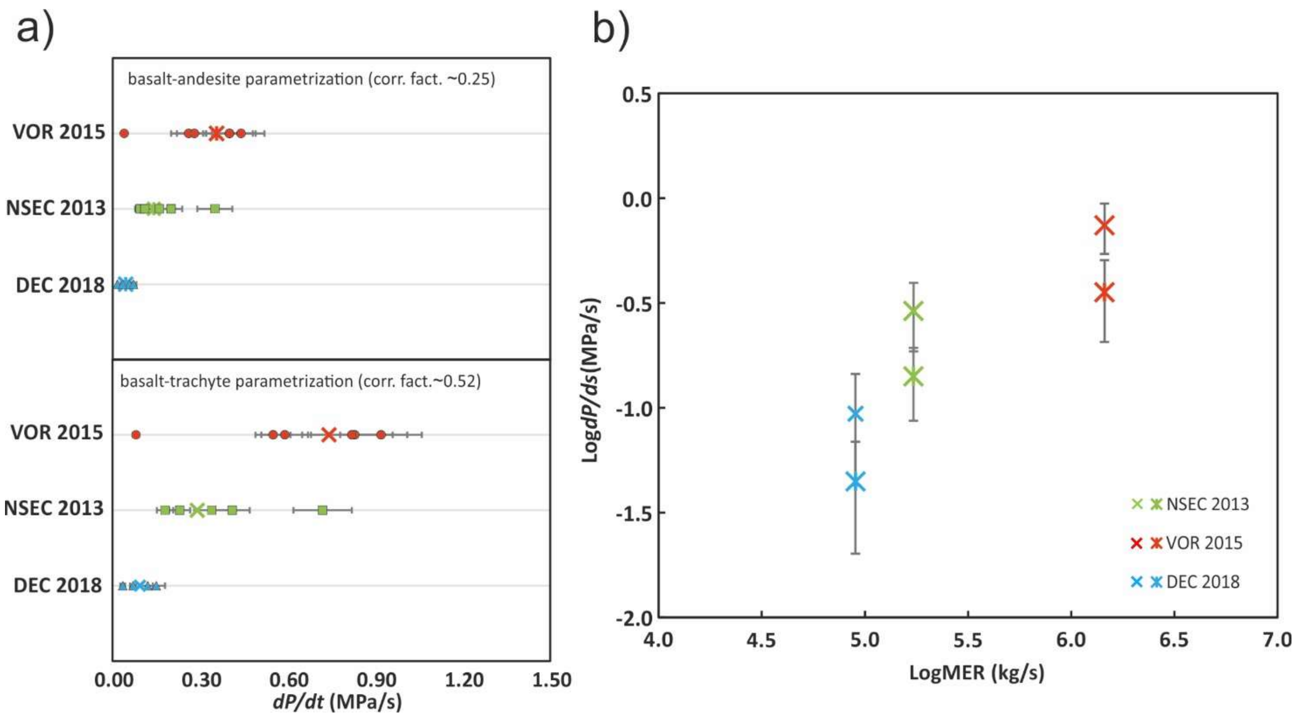

Figure 8. a) Results of decompression rates estimated using the two distinct basalt-andesite and basalt-trachyte parametrizations. Symbols are as shown in Figure 6; stars are averaged decompression rates calculated for the basalt-andesite, while crosses are averaged decompression rates calculated for the basalt-trachyte (outliers are not taken into account in the estimation of averaged values); b) MER vs. *dP/dt,* expressed as logarithm, showing the relationship between explosivity and decompression rate (symbols as in panel a).

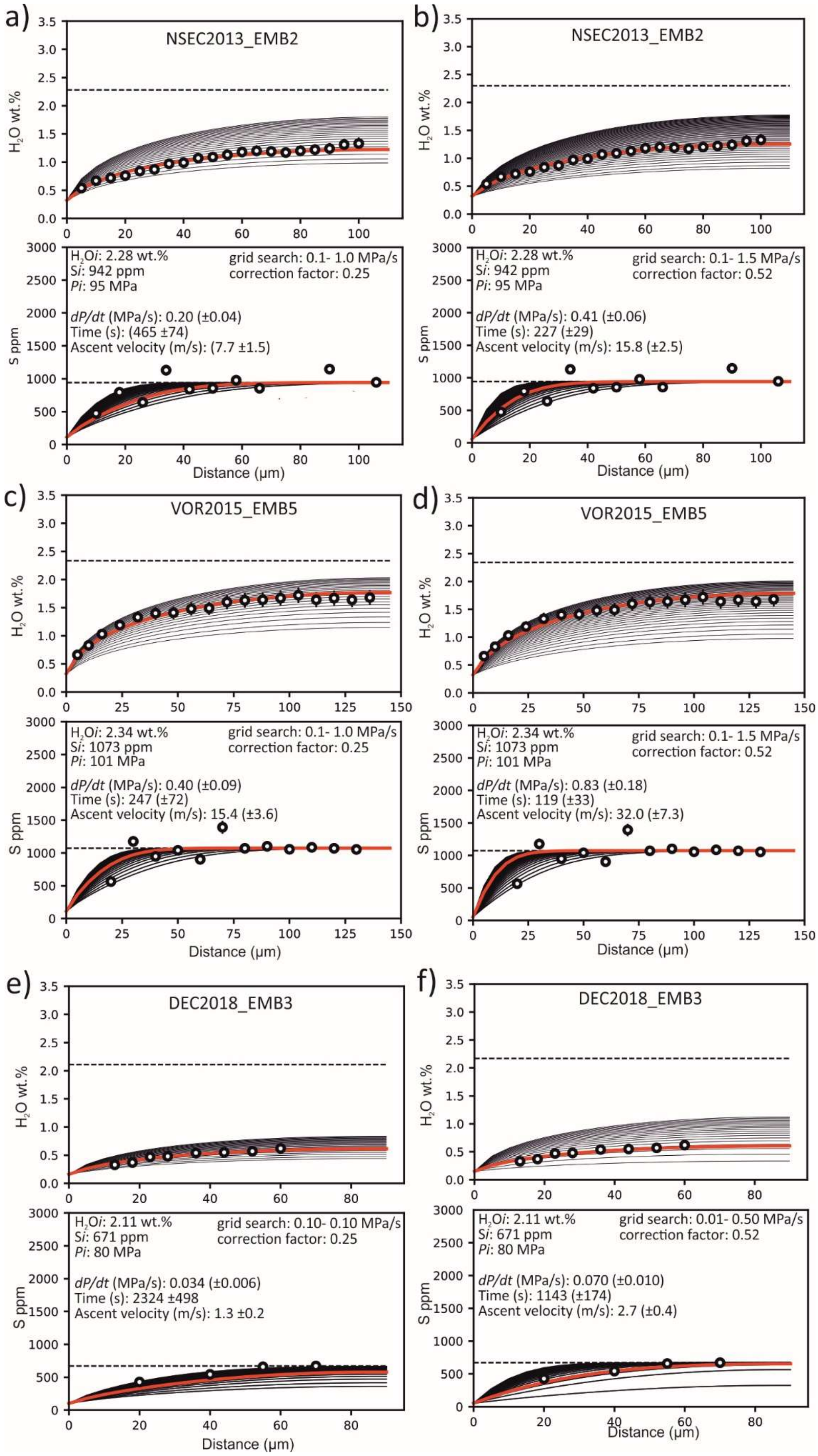
a)
NSEC2013_EMB2
H2O wt.%
H2Oi: 2.28 wt.%
Si: 942 ppm
Pi: 95 MPa
grid search: 0.1- 1.0 MPa/s
correction factor: 0.25
dP/dt (MPa/s): 0.20 (±0.04)
Time (s): (465 ±74)
Ascent velocity (m/s): (7.7 ±1.5)
S ppm
Distance (µm)
b)
NSEC2013_EMB2
H2O wt.%
H2Oi: 2.28 wt.%
Si: 942 ppm
Pi: 95 MPa
grid search: 0.1- 1.5 MPa/s
correction factor: 0.52
dP/dt (MPa/s): 0.41 (±0.06)
Time (s): 227 (±29)
Ascent velocity (m/s): 15.8 (±2.5)
S ppm
Distance (µm)
c)
VOR2015_EMB5
H2O wt.%
H2Oi: 2.34 wt.%
Si: 1073 ppm
Pi: 101 MPa
grid search: 0.1- 1.0 MPa/s
correction factor: 0.25
dP/dt (MPa/s): 0.40 (±0.09)
Time (s): 247 (±72)
Ascent velocity (m/s): 15.4 (±3.6)
S ppm
Distance (µm)
d)
VOR2015_EMB5
H2O wt.%
H2Oi: 2.34 wt.%
Si: 1073 ppm
Pi: 101 MPa
grid search: 0.1- 1.5 MPa/s
correction factor: 0.52
dP/dt (MPa/s): 0.83 (±0.18)
Time (s): 119 (±33)
Ascent velocity (m/s): 32.0 (±7.3)
S ppm
Distance (µm)
e)
DEC2018_EMB3
H2O wt.%
H2Oi: 2.11 wt.%
Si: 671 ppm
Pi: 80 MPa
grid search: 0.10- 0.10 MPa/s
correction factor: 0.25
dP/dt (MPa/s): 0.034 (±0.006)
Time (s): 2324 ±498
Ascent velocity (m/s): 1.3 ±0.2
S ppm
Distance (µm)
f)
DEC2018_EMB3
H2O wt.%
H2Oi: 2.11 wt.%
Si: 671 ppm
Pi: 80 MPa
grid search: 0.01- 0.50 MPa/s
correction factor: 0.52
dP/dt (MPa/s): 0.070 (±0.010)
Time (s): 1143 (±174)
Ascent velocity (m/s): 2.7 (±0.4)
S ppm
Distance (µm)

Figure 9. Representative results from volatile diffusion modeling along melt-embayments found in the selected post-2011 eruptions, using the basalt-andesite (a,c,d) and basalt-trachyte (b,d,f) parametrizations for D_{H2O} correction. Red line represents the best fit model corresponding to the estimated *dP/dt* by χ^2 minimization, starting from fixed initial P_i, S_i and H_2O_i (black dashed line) at constant T_i = 1080 °C; thin black lines represent individual simulations for different *dP/dt* values defined in the search grid used to minimize χ^2 at the same fixed conditions.

Table 1. Results from volatile diffusion modeling on melt embayments of NSEC 2013, VOR 2015 and DEC 2018 eruptions at Mt. Etna.

	H_2O_i (wt.%)	S_i (ppm)*	P_i (MPa)	P_f (MPa)	dP/dt (MPa/s ±2σ) $k_1 = 0.25$**	v (m/s ±2σ) $k_1 = 0.25$	dP/dt (MPa/s ±2σ) $k_2 = 0.52$	v (m/s ±2σ) $k_2 = 0.52$	t (min)	χ^2 (k_1 / k_2)
NSEC_emb1	2.21	825	89	1	0.16 (±0.03)	6.2 (±1.1)	0.34 (±0.06)	13.1 (±2.4)	4.3-9.2	21.4 / 13.1
NSEC_emb2	2.28	942	95	2	0.20 (±0.04)	7.7 (±1.5)	0.41 (±0.06)	15.8 (±2.5)	3.8-7.8	4.2 / 4.2
NSEC_emb3	1.88	412	62	1	0.094 (±0.018)	3.5 (±0.6)	0.18 (±0.03)	6.9 (±1.2)	5.6-11.3	10.0 / 10.0
NSEC_emb4	2.15	724	83	2	0.35 (±0.06)	13.5 (±2.4)	0.72 (±0.10)	27.7 (±4.1)	1.9-3.9	1.6 / 1.6
NSEC_emb5	2.25	888	92	1	0.11 (±0.02)	4.2 (±1.0)	0.23 (±0.036)	8.8 (±1.5)	6.6-13.8	9.3 / 9.3
Average***					0.14 (±0.10)	7.9 (±4.0)	0.29 (±0.10)	11.2 (±4.0)	4.4-9.2	
VOR_emb1	2.41	1245	108	1	0.26 (±0.06)	10.0 (±2.4)	0.55 (±0.06)	22.0 (±3.3)	3.1-6.9	14.3 / 14.2
VOR_emb2	2.30	992	97	1	0.039 (±0.008)	1.5 (±0.3)	0.08 (±0.01)	3.1 (±0.4)	19.8-41.0	54.9 / 55.0
VOR_emb3	2.31	999	98	1	0.28 (±0.06)	10.8 (±2.4)	0.59 (±0.08)	23.2 (±3.8)	2.7-5.8	22.9 / 22.6
VOR_emb4	2.30	989	97	2	0.44 (±0.08)	16.9 (±3.2)	0.92 (±0.14)	35.4 (±5.7)	1.7-3.6	5.4 / 5.5
VOR_emb5	2.34	1073	101	2	0.40 (±0.09)	15.4 (±3.6)	0.83 (±0.18)	32.0 (±7.3)	2.0-4.1	8.4 / 8.5
VOR_emb6	2.28	956	95	1	0.40 (±0.08)	15.4 (±3.2)	0.82 (±0.14)	31.5 (±5.7)	1.9-3.9	14.7 / 14.6
Average****					0.36 (±0.08)	13.7 (±3.1)	0.74 (±0.16)	28.8 (±5.9)	2.3-4.9	
DEC_emb1	2.29	965	96	1	0.057 (±0.012)	2.2 (±0.5)	0.12 (±0.018)	4.7 (±0.8)	13.1-27.8	1.9 / 1.9
DEC_emb2	2.12	686	81	1	0.016 (±0.002)	0.6 (±0.1)	0.035 (±0.008)	1.3 (±0.3)	38.6-83.3	4.0 / 4.0
DEC_emb3	2.11	671	80	1	0.034 (±0.006)	1.3 (±0.2)	0.07 (±0.01)	2.7 (±0.4)	19.1-38.7	4.3 / 4.3
DEC_emb4	2.18	773	86	1	0.071 (±0.010)	2.7 (±0.4)	0.15 (±0.03)	5.6 (±1.0)	9.8-20.0	5.4 / 5.4
Average					0.045 (±0.024)	1.7 (±0.9)	0.094 (±0.051)	3.6 (±1.9)	20.1-42.4	

* S initial concentrations are average values considering the first 1-4 spots measured in the embayments interior.

** k_1, k_2 are correction factors linked respectively to the basalt-andesite and basalt-trachyte parametrizations.

*** Sample NSEC 2013_emb3 is not considered in the calculation of average values.

**** Sample VOR2015_emb2 is not considered in the calculation of average values.